ACS OMEGA

Open Access



http://pubs.acs.org/journal/acsodf

Article

# Continuously Adjustable Thickness of $Bi_2MoO_6$ Nanosheets Enhances Photocatalytic Oxidation

Hongjuan Yun,* Qingguo Gao, Yin Yan, Yin Yu, Yuanyuan Zhang, and Chun Li*

Cite This: *ACS Omega* 2024, 9, 22459−22465

Read Online

ACCESS | Metrics & More | Article Recommendations | Supporting Information

**ABSTRACT:** In this study, two-dimensional (2D) nanosheet photocatalysts of $Bi_2MoO_6$ with varying thicknesses were synthesized by adjusting the temperature during the hydrothermal reaction. The thinnest $Bi_2MoO_6$ nanosheet reached an approximate thickness of ∼4 nm, while the thickest nanosheet measured only ∼16 nm. The photocatalytic performance for Rhodamine B (RhB) degradation was found to be the most effective for the thinnest $Bi_2MoO_6$ nanosheet, displaying a degradation rate constant of 0.11 $min^{-1}$. This rate was 2.5 times higher than that observed for the ∼16 nm thick $Bi_2MoO_6$ photocatalyst. The enhanced performance of the thinner two-dimensional nanostructure can be attributed to improved separation and migration of photogenerated charges. Additionally, the study identified hydroxyl radicals (•OH) and superoxide radicals ($\bullet O_2^-$) as crucial oxidative species, contributing to the efficient mineralization of RhB dye. This work highlights the controllable synthesis of 2D materials with varying thicknesses and their specific applications in photocatalytic oxidation.

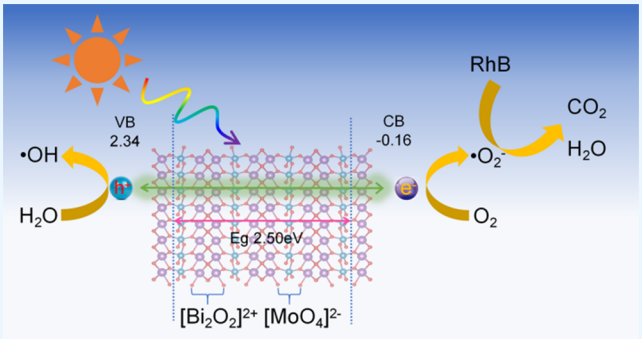


## 1. INTRODUCTION

The efficient, clean, and sustainable treatment of printing and dyeing wastewater has consistently posed challenges in the textile and printing and dyeing industry.[1−3] Currently, prevalent methods for treating printing and dyeing wastewater include biological treatment, physical treatment, and chemical treatment.[4−6] However, these existing methods encounter significant issues. For instance, the microorganisms relied upon in biological treatment are highly susceptible to environmental conditions, temperature fluctuations, and water quality.[7] Physical treatment methods are energy-intensive and fall short of completely mineralizing contaminants.[8] Chemical treatment mandates the use of large quantities of chemical reagents, resulting in resource consumption.[9] Consequently, there is a growing focus on low-cost, environmentally friendly methods for treating printing and dyeing wastewater.[10] Inorganic semiconductor photocatalysts, when exposed to light excitation, generate reactive oxygen species with potent oxidation capabilities, facilitating the mineralization of most pollutants.[11] The utilization of inorganic semiconductor photocatalytic technology has emerged as a representative approach for achieving clean, green, and sustainable processes in the treatment of printing and dyeing wastewater.[12]

Photocatalytic oxidation technology effectively degrades pollutants in printing and dyeing wastewater without the addition of extra chemical reagents, utilizing solar energy as its energy source.[13] It is a green, environmentally friendly process with low energy consumption. However, the efficiency of photocatalytic oxidation technology is heavily reliant on photocatalysts. In fact, factors such as photocatalyst light absorption, charge separation, and surface redox sites can significantly impact the degradation efficiency of pollutants in printing and dyeing wastewater.[14] Among these influencing factors, charge separation and migration are crucial and have consistently restricted the efficiency of photocatalytic degradation.[15] Therefore, with the prerequisite of ensuring that the photocatalyst possesses the capability to degrade printing and dyeing wastewater, enhancing the separation efficiency and migration rate of photocatalyst charges to the greatest extent possible has become a critical research focus in the advancement of efficient photocatalytic oxidation technology.

Two-dimensional (2D) materials, exemplified by graphene, have garnered significant attention owing to their excellent electron transfer capabilities.[16] Additionally, 2D materials offer significant advantages in photogenerated charge separation and migration. First, the higher specific surface area provides more opportunities for light absorption, increasing the probability of generating photogenerated electron−hole pairs.[17,18] Second, due to the thin thickness of 2D materials, the migration paths of electrons and holes within the material are very short, reducing

Received: March 15, 2024
Revised: April 16, 2024
Accepted: April 30, 2024
Published: May 9, 2024

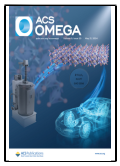

the possibility of recombination and contributing to the long life of photogenerated charges.[19] Moreover, some single-layer 2D semiconductor materials exhibit a direct energy gap structure, implying that the energy of electrons and holes within the band gap is relatively small, facilitating the separation of photogenerated charges.[20] Simultaneously, the optoelectronic structure of 2D materials may feature special energy band structures, such as Dirac points or Dirac cones, providing additional support for the effective separation and migration of photogenerated charges.[21] Finally, carriers in 2D materials generally exhibit higher mobility within the crystal lattice, allowing them to move more rapidly through the material and minimizing the chance of recombination.[22] Consequently, regulating the structure of the photocatalyst to transform it into a 2D material and adjusting its 2D thickness proves to be an effective means of promoting charge separation and migration.

Here, we synthesized $Bi_2MoO_6$ 2D nanosheet photocatalysts with varying thicknesses by controlling the temperature during the hydrothermal reaction. The thinnest $Bi_2MoO_6$ 2D nanosheet photocatalyst achieved a thickness of ∼4 nm. These $Bi_2MoO_6$ 2D nanosheet photocatalysts with different thicknesses exhibited high photocatalytic oxidation performance, effectively achieving complete degradation and mineralization of printing and dyeing wastewater within 1 h. Notably, the degradation rate constant of $Bi_2MoO_6$ 2D nanosheets with an ∼4 nm thickness reached 0.11 $min^{-1}$, which is 2.5 times that of the $Bi_2MoO_6$ 2D nanosheets with an ∼16 nm thickness. The thinner 2D structure facilitated the separation and migration of photogenerated charges, leading to the generation of reactive oxygen species, including hydroxyl radicals and superoxide radicals. This process resulted in the complete removal of the Rhodamine B (RhB) pollutant in printing and dyeing wastewater.

## 2. EXPERIMENTAL SECTION

**2.1. Reagents.** Hexadecyltrimethylammonium bromide [$CH_3(CH_2)_{15}N(Br)(CH_3)_3$, ≥98%], bismuth(III) nitrate pentahydrate [$Bi(NO_3)_3{\cdot}5H_2O$, ACS reagent, ≥98.0%], sodium molybdate dihydrate [$Na_2MoO_4{\cdot}2H_2O$, ACS reagent, ≥99%], and chloroplatinic acid hexahydrate were purchased from Sigma-Aldrich Chemical Reagent Co. Ltd.

**2.2. Catalyst Preparation.** The ultrathin $Bi_2MoO_6$ nanosheets were synthesized through a straightforward hydrothermal reaction. Specifically, 1 mmol of $Na_2MoO_4{\cdot}2H_2O$, 2 mmol of $Bi(NO_3)_3{\cdot}5H_2O$, and 0.05 g of hexadecyltrimethylammonium bromide (CTAB) were added to 80 mL of deionized water and stirred for 30 min. The mixed solution was then transferred into a 100 mL Teflon-lined autoclave, sealed in a stainless steel tank, and subjected to hydrothermal reaction. The hydrothermal temperature was maintained at 140, 120, 110, 100, 90, and 80 °C for 24 h, respectively. Finally, the product was collected, washed several times with deionized water, and dried at 70 °C in air for 12 h. The resulting samples were labeled as BMO-140, BMO-120, BMO-110, BMO-100, BMO-90, and BMO-80 according to the respective hydrothermal temperatures.

**2.3. Photocatalytic RhB Degradation.** First, a solution of RhB with a concentration of 10 mg/L was prepared. Then, 30 mL of the solution was added to the photocatalytic degradation reactor followed by 30 mL of water and 60 mg of catalyst. The mixture was stirred in the dark for half an hour until catalyst adsorption equilibrium was reached. A 300 W xenon lamp (PLS-SXE300/300UV, Beijing Perfectlight Technology Co. Ltd.) with a UV cutoff filter ($\lambda \geq 420$ nm) was used for photocatalytic degradation of RhB under simulated visible sunlight. Samples were taken every 10 min from the beginning of light until RhB was completely degraded. The RhB solution obtained during the degradation process was centrifuged, and the centrifuged solution was measured for absorption spectrum using an ultraviolet−visible spectrophotometer to determine the degradation process of RhB at its maximum absorption wavelength (554 nm). The degradation rate of the catalyst to RhB can be calculated using eq 1 to evaluate the photocatalytic activity of the catalyst.

$$D = [(A_0 - A)/A_0] \times 100\% \quad (1)$$

The measurement parameters of the ultraviolet−visible spectrophotometer (model: TU-1901 double light velocity) were as follows: the scanning range was 200−800 nm, the wavelength repeatability was ≤0.1 nm, and the scanning speed was 2 nm $s^{-1}$. The solution was quantitatively analyzed based on Lambert−Beer's law, which states that $A = \varepsilon bc$ (where $A$ is the absorbance, $\varepsilon$ is the molar absorptivity, $b$ is the thickness of the liquid pool, and $c$ is the solution concentration).

**2.4. Characterizations.** The catalyst's crystal phase structure was verified using X-ray diffractometry (XRD) with Cu−K$\alpha$ irradiation ($\lambda$ = 1.5406 Å). Raman spectroscopy was conducted using the Inva-Reflex Micro-Raman Spectroscopy System 1000, employing a 532 nm solid-state laser for excitation across the 100−2000 $cm^{-1}$ wavenumber range. Spectral resolution was ≤1 $cm^{-1}$ for the visible spectrum and ≤2 $cm^{-1}$ for the ultraviolet spectrum. Morphological and crystal structure analyses were performed using field emission scanning electron microscopy (FE-SEM, JEOL JS-6701F) and field emission transmission electron microscopy (FETEM, Talos F200S). The catalyst's electronic structure was examined through X-ray photoelectron spectroscopy (XPS), calibrated to the C 1s peak at 284.8 eV. The specific surface area was determined by nitrogen adsorption−desorption isotherm tests at 77 K using a Micromeritics ASAP 2020 apparatus, followed by Brunauer−Emmett−Teller (BET) analysis. UV−vis diffuse reflectance spectra (UV−vis DRS) were acquired with a Varian Cary 500 UV−vis spectrometer, using $BaSO_4$ powder as a reference, and scanning from 200 to 800 nm at a speed of 200 nm $min^{-1}$. Electron paramagnetic resonance (EPR) spectroscopy measurements were conducted at room temperature using a Bruker A300 EPR spectrometer. DMPO served as a capture agent to detect hydroxyl radicals and superoxide radicals, respectively. Water and methanol were used as solvents to detect hydroxyl radicals and superoxide radicals, respectively. Initially, 2.5 mg of photocatalyst was dispersed in 0.5 mL of water or methanol, respectively. Subsequently, 20 $\mu$L of DMPO solution was added. After thorough mixing of the mixture, a certain amount of the mixed solution was absorbed using a capillary tube, and both ends of the capillary tube were sealed with plasticine. Finally, the sealed capillary tube was placed in an EPR test tube for analysis and in a liquiTOC II total organic carbon analyzer for total organic carbon testing.

**2.5. Photoelectrochemical Characterization.** To prepare the working electrode, the catalyst was dispersed in ethanol using ultrasonication. The resulting mixed solution was then deposited onto fluorine-doped tin oxide (FTO) conductive glass and air-dried. Photoelectrochemical experiments were conducted in a three-electrode system using a CHI-660D workstation, with an Ag/AgCl electrode as the reference electrode and a graphite sheet as the counter electrode. The photocurrent test employed a 0.2 M $Na_2SO_4$ solution as the


https://doi.org/10.1021/acsomega.4c02493
ACS Omega 2024, 9, 22459−22465

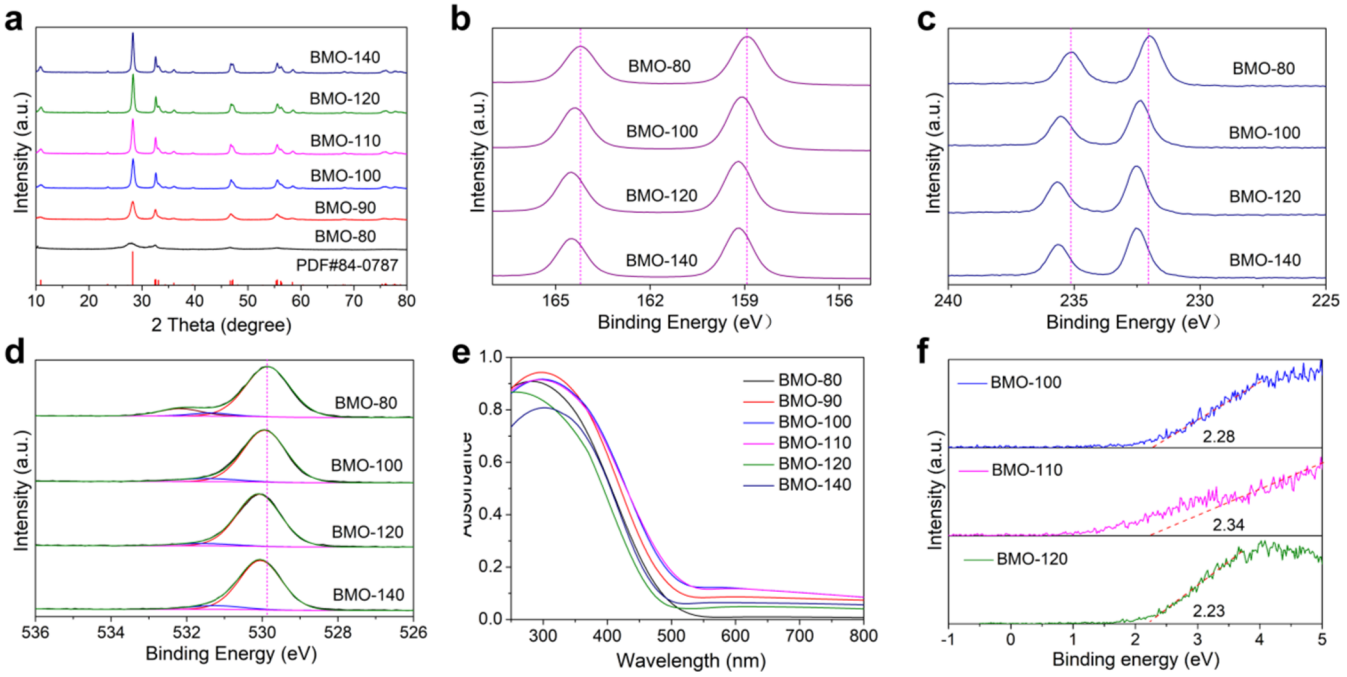


**Figure 1.** (a) XRD patterns of $Bi_2MoO_6$ samples prepared at various temperatures. XPS spectra of $Bi_2MoO_6$ samples prepared at various temperatures: (b) XPS spectra of Bi 4f, (c) XPS spectra of Mo 3d, and (d) XPS spectra of O 1s. (e) UV−vis DRS and (f) XPS-VB spectra of $Bi_2MoO_6$ samples prepared at various temperatures.

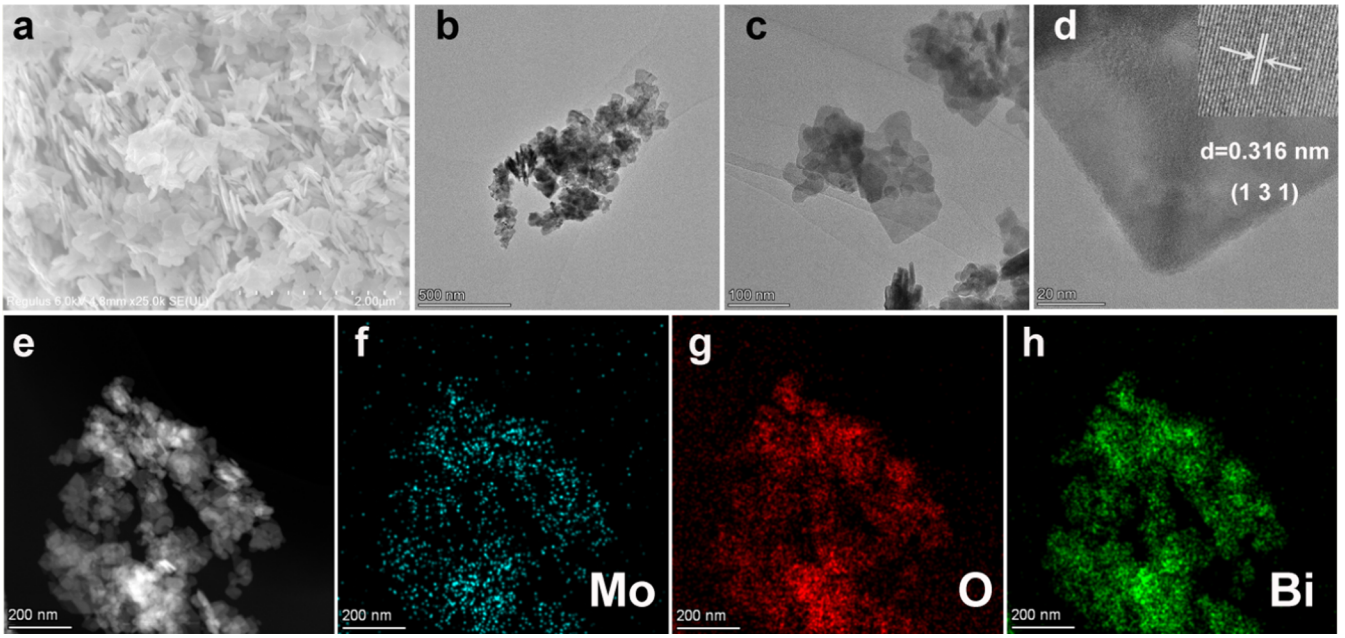


**Figure 2.** (a) SEM image of BMO-110. (b) TEM image of BMO-110 with a scale bar of 500 nm. (c) TEM image of BMO-110 with a scale bar of 100 nm. (d) HRTEM image of BMO-110. (e−h) EDX elemental mapping images.

electrolyte, and a Xe lamp served as the simulated light source. Electrochemical impedance spectroscopy (EIS) experiments were performed in a mixed solution containing 0.5 M KCl and 5.0 mM $K_3[Fe(CN)_6]/K_4[Fe(CN)_6]$.

## 3. RESULTS AND DISCUSSION

**3.1. Composition and Structural Characterization.** $Bi_2MoO_6$ nanosheet photocatalysts with different thicknesses were prepared using a simple one-step hydrothermal method. The XRD diffraction peaks of the samples, prepared under different temperature conditions, correspond one-to-one with the standard XRD diffraction peaks of orthorhombic $Bi_2MoO_6$ (PDF#84-0787).[23] No diffraction peaks of any other impurities were observed, indicating high sample purity, as shown in Figure 1a. Moreover, as the preparation reaction temperature increases, the crystallinity of the sample also gradually increases. It is noteworthy that the poor crystallinity of the BMO-80 sample is attributed to the lower preparation temperature.[24] Additionally, the elemental composition and valence state of samples synthesized under different temperature conditions were


https://doi.org/10.1021/acsomega.4c02493
ACS Omega 2024, 9, 22459−22465

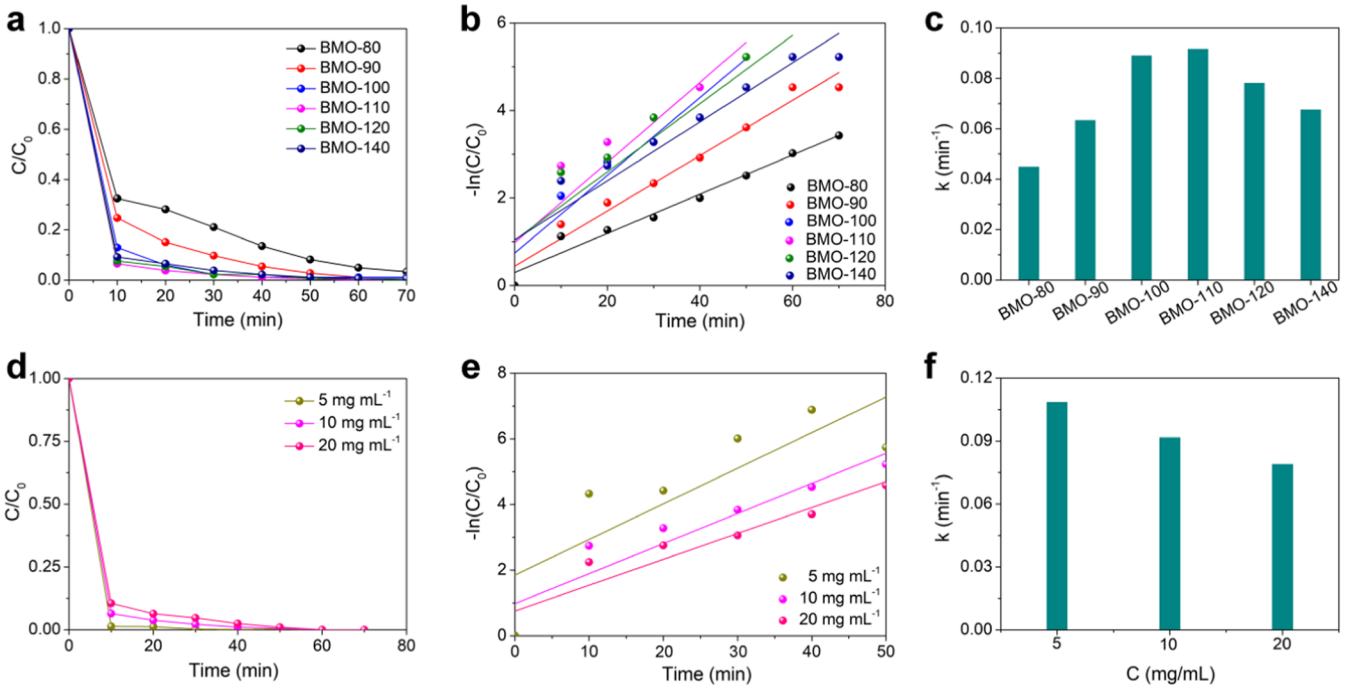


**Figure 3.** Visible light photocatalytic degradation of RhB was studied by investigating: (a) degradation curves of a series of catalysts under light irradiation, (b) the corresponding $\ln(C_0/C) - t$ values; and (c) the reaction rate constants. (d) Degradation curves of different RhB concentrations and (e) the corresponding $\ln(C_0/C) - t$ as well as (f) reaction rate constants.

explored through XPS. A set of double peaks with binding energies of 158.92 and 164.21 eV were assigned to the XPS peaks of Bi $4f_{7/2}$ and Bi $4f_{5/2}$ of the BMO-80 photocatalyst, indicating a valence state of Bi as +3.[25] As the reaction temperature increases, the XPS double peaks of Bi $4f_{7/2}$ and Bi $4f_{5/2}$ gradually shift toward higher binding energy, as shown in Figure 1b, possibly due to enhanced crystallinity. The double peaks with binding energies of 232.02 and 235.15 eV belong to the XPS peaks of Mo $3d_{5/2}$ and Mo $3d_{3/2}$ of the BMO-80 photocatalyst, as shown in Figure 1c, indicating a valence state of Mo as +6.[26] It was observed that as the sample preparation temperature increases, the XPS double peaks of Mo $3d_{5/2}$ and Mo $3d_{3/2}$ gradually shift toward higher binding energy. For BMO-80, the XPS peaks with binding energies of 529.87, 531.40, and 532.19 eV belong to the XPS peaks of lattice oxygen, surface hydroxyl groups, and surface-adsorbed oxygen species, respectively.[27−29] As the catalyst preparation temperature increases, the XPS peaks of surface-adsorbed oxygen species gradually disappear. Simultaneously, the XPS diffraction peak attributed to lattice oxygen also shows a shift toward higher binding energy, as shown in Figure 1d. The UV−visible diffuse reflectance spectrum shows that the band gap value of the sample under a series of different temperature preparation conditions is between 2.51 and 2.63 eV.[30] Since the band gap values are all less than 2.95 eV, it means that the samples all have the ability to absorb visible light. Finally, valence band XPS was used to test the valence band potential of the photocatalyst, as shown in Figure 1f. Obviously, the valence band edges of the series of photocatalysts are estimated to be +2.23, +2.34, and +2.28 eV below the Fermi level, respectively, by linear extrapolation. In addition, the conduction band edges of the series of photocatalysts are located at −0.23, −0.16, and −0.40 eV, respectively, obtained by $E_g = E_{VB} - E_{CB}$, where $E_g$ is the semiconductor band gap; $E_{VB}$ is the valence band edge potential; and $E_{CB}$ is the conduction band edge potential.[31]

**3.2. Morphological Characterization.** SEM and TEM are employed for the analysis and observation of the micromorphology of catalysts. SEM indicates that BMO-110 exhibits the fundamental morphology of 2D nanosheets with a high dispersion between them (Figure 2a). Simultaneously, TEM, at various magnifications, reveals the 2D nanosheet structure of the BMO-110 sample (Figure 2b,2c). Additionally, AFM reveals that the thicknesses of BMO-80, BMO-90, BMO-100, BMO-110, BMO-120, and BMO-140 are approximately ∼16, ∼12, ∼6, ∼4, ∼8, and ∼9 nm, respectively (Figure S1). Clearly, BMO-110 has the thinnest size, which is advantageous for the separation and migration of photogenerated charges. HRTEM distinctly shows 0.316 nm lattice fringes, corresponding to the (1 3 1) crystal plane of $Bi_2MoO_6$ (Figure 2d). Furthermore, the elemental mapping images (Figure 2e−2h) distinctly depict the uniform distribution of each element. This further affirms the successful preparation of high-quality $Bi_2MoO_6$ 2D nanosheets. Nitrogen physical adsorption measurements show that the specific surface area of BMO-80, BMO-90, BMO-100, BMO-110, BMO-120, and BMO-140 are 8.4, 12.6, 18.9, 32.6, 28.4, and 27.6 $cm^2\ g^{-1}$, respectively (Figure S2).

**3.3. Photocatalytic RhB Degradation.** The photocatalytic performance of a series of $Bi_2MoO_6$ photocatalysts and *P*25 samples with different thicknesses was evaluated through visible light photocatalytic RhB dye degradation experiments. The blank experiment without adding any photocatalyst showed that RhB did not undergo obvious self-degradation under visible light irradiation. Since the band gap of *P*25 is about 3.1−3.2 eV and cannot be excited by visible light, it fails to show photocatalytic degradation performance for RhB (Figure S3).[32] A series of $Bi_2MoO_6$ photocatalysts with different thicknesses exhibit visible light photocatalytic RhB degradation performance due to their ability to absorb visible light. For $Bi_2MoO_6$ photocatalysts with different thicknesses, complete degradation of RhB can be achieved basically within 70 min, as


https://doi.org/10.1021/acsomega.4c02493
ACS Omega 2024, 9, 22459−22465

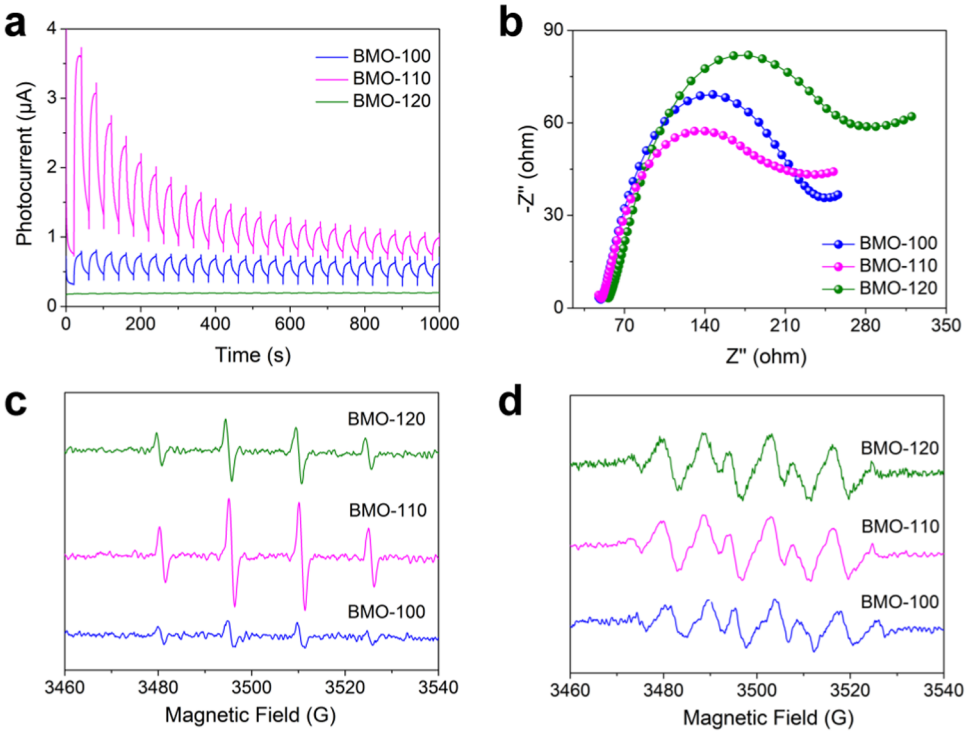


**Figure 4.** (a) Photocurrent response test with periodic on/off cycles. (b) Impedance Nyquist plots of the samples. EPR signals for (c) DMPO−•OH and (d) TMPO−$•O_2^-$.

shown in Figure 3a. Especially for BMO-110, the degradation efficiency of RhB can reach 93.5% within 10 min, which is much higher than the degradation efficiency of BMO-80 (67.6%) for RhB within 10 min. When testing total organic carbon, 10 min, the RhB mineralization can reach 46.9%. The reason why BMO-110 has the best photocatalytic performance may be its thinnest thickness, which is beneficial to the separation of photogenerated charges. The order of photocatalytic effects of the series of photocatalysts on RhB dyes is BMO-110 > BMO-120 > BMO-140 > BMO-100 > BMO-90 > BMO-80. Increasing the concentration of RhB further to 50 mg $L^{-1}$, the photocatalytic performance of the series of photocatalysts on RhB dyes follows the order of BMO-110 > BMO-140 > BMO-90 > BMO-80 (Figure S4). In addition, the degradation kinetics curve of the photocatalyst RhB conforms to the pseudo-first-order linear transformation $\ln(C_0/C) = kt$, as shown in Figure 3b. At the same time, the RhB degradation rate constants of the series of photocatalysts showed a typical volcano-type law, as shown in Figure 3c. The pseudo-first-order reaction kinetic rate constant of the BMO-110 sample reached 0.092 $min^{-1}$, which is twice that of the BMO-80 sample (0.045 $min^{-1}$). Additionally, the degradation performance of BMO-110 samples to different concentrations of RhB was also studied, as shown in Figure 3d. As the concentration of the RhB solution increases, the time required for degradation also increases. Despite this, BMO-110 can achieve 100% degradation of RhB at different concentrations within a specific time frame. The kinetic curves of BMO-110 degradation by RhB at different concentrations also conform to the pseudo-first-order linear transformation $-\ln(C_0/C) = kt$ (Figure 3e). The pseudo-first-order reaction kinetics of 5, 10, and 20 mg/mL RhB solutions were 0.108, 0.09, and 0.078 $min^{-1}$, respectively (Figure 3f). Three cycles of experimental testing show that the BMO-110 photocatalyst has excellent photocatalytic stability. Each cycle was completed within 60 min, essentially achieving complete degradation of RhB (Figure S5). The crystalline phase structure and light absorption of the catalyst did not change significantly before and after the reaction, indicating that the catalyst has good stability (Figures S6−S8).

**3.4. Photoelectric and Radical Characterization.** To elucidate the differences in the photocatalytic properties of $Bi_2MoO_6$ 2D nanosheets with different thicknesses, the separation efficiency and migration rate of carriers were evaluated through photoelectric and fluorescence tests. Clearly, the BMO-110 2D nanosheet photocatalyst, with the smallest thickness, exhibits the highest photocurrent density and the smallest electrochemical impedance radius compared to other samples, as shown in Figure 4a,4b.[33] At the same time, BMO-110 also exhibited the lowest fluorescence intensity and longer fluorescence lifetime (Figures S9 and S10). This indicates that the BMO-110 sample has the best photogenerated charge separation efficiency and migration rate. Thinner 2D materials, due to their reduced thickness, can significantly enhance carrier separation and shorten the distance of carrier migration. Consequently, photogenerated charges quickly migrate to the surface of the catalyst to undergo redox reactions. Additionally, EPR was employed to detect reactive intermediates of oxidation reactions during the process. •OH and $•O_2^-$ were successfully detected as important intermediates, as shown in Figure 4c,4d.[34] Meantime, compared with other samples, the BMO-110 2d nanosheet photocatalyst with the smallest thickness also exhibited the strongest EPR signals of •OH and $•O_2^-$. Therefore, it possesses the best photocatalytic activity. •OH and $•O_2^-$ are crucial intermediate active substances capable of oxidizing RhB to $CO_2$ and $H_2O$. Hence, the addition of a •OH masking agent, *tert*-butyl alcohol, and a $•O_2^-$ masking agent, p-benzoquinone, during the RhB degradation process determined the main intermediates for the photocatalytic degradation of


https://doi.org/10.1021/acsomega.4c02493
ACS Omega 2024, 9, 22459−22465

RhB by the $Bi_2MoO_6$ 2D nanosheet photocatalyst. As shown in Figure S11, the addition of tert-butanol only delayed the degradation time, while the addition of the p-benzoquinone masking agent resulted in incomplete degradation of RhB. This suggests that $\bullet O_2^-$ may be the primary intermediate for the photocatalytic degradation of RhB by the $Bi_2MoO_6$ 2D nanosheet photocatalyst.

**3.5. Photocatalytic Mechanism.** Building upon the preceding discussion, we propose the mechanism for the photocatalytic degradation of RhB by bismuth molybdate nanosheets, illustrated in Figure 5. $Bi_2MoO_6$ constitutes a

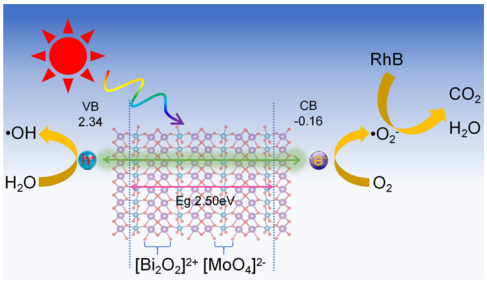


**Figure 5.** Diagrammatic representation of the photocatalytic degradation mechanism of RhB using $Bi_2MoO_6$ Nanosheets. The background crystal structure was created by VESTA program.[35]

layered material, comprising $[Bi_2O_2]^{2+}$ layers and corner-sharing $[MoO_6]^{2-}$ octahedral layers. $Bi_2MoO_6$ nanosheets exhibit either a sandwich structure of $[BiO]^+-[MoO_6]^{2-}-[BiO]^+$ or a nonsandwich structure of $[Bi_2O_2]^{2+}-[MoO_6]^{2-}$. In the presence of illumination, $Bi_2MoO_6$ nanosheets undergo excitation by light, resulting in the generation of photogenerated electrons and holes. The ultrathin 2D structure facilitates the efficient separation and migration of these photogenerated charges. Consequently, photogenerated electrons engage with surface $O_2$ to produce $\bullet O_2^-$, whereas photogenerated holes oxidize $H_2O$ into •OH. The robust oxidizing capacity of •OH and $\bullet O_2^-$ leads to the further mineralization of the RhB dye into $CO_2$ and $H_2O$.

## 4. CONCLUSIONS

Through the adjustment of the hydrothermal reaction temperature, a series of 2D $Bi_2MoO_6$ nanosheet photocatalysts with varying thicknesses were successfully synthesized. The thinnest $Bi_2MoO_6$ nanosheets measure approximately ∼4 nm in thickness, while the thickest nanosheets are only ∼16 nm thick. Notably, the thinnest $Bi_2MoO_6$ nanosheets exhibit the most efficient photocatalytic degradation of Rhodamine B, boasting a degradation rate constant of 0.11 $min^{-1}$. This value is 2.5 times greater than the degradation rate of the $Bi_2MoO_6$ photocatalyst with a thickness of ∼16 nm. The thin 2D nanostructures play a crucial role in facilitating the separation and migration of photogenerated charges. Additionally, $\bullet O_2^-$, identified as the primary active intermediate, effectively drives the mineralization of RhB.

## ■ ASSOCIATED CONTENT

### Supporting Information

The Supporting Information is available free of charge at https://pubs.acs.org/doi/10.1021/acsomega.4c02493.

Characterization of catalyst, catalyst stability, and photocatalytic experiments (PDF)

## ■ AUTHOR INFORMATION


### Corresponding Authors

**Hongjuan Yun** − *Xinjiang Academy of Environmental Protection Science, Urumqi, Xinjiang 830011, China; Xinjiang Engineering Technology Research Center for Cleaner Production, Urumqi, Xinjiang 830011, China;* orcid.org/0009-0000-6228-0835; Email: 1012927795@qq.com

**Chun Li** − *Xinjiang Academy of Environmental Protection Science, Urumqi, Xinjiang 830011, China; Xinjiang Engineering Technology Research Center for Cleaner Production, Urumqi, Xinjiang 830011, China;* Email: 285655035@qq.com

### Authors

**Qingguo Gao** − *Xinjiang Academy of Environmental Protection Science, Urumqi, Xinjiang 830011, China; Xinjiang Engineering Technology Research Center for Cleaner Production, Urumqi, Xinjiang 830011, China*

**Yin Yan** − *Xinjiang Institute of Technology, Urumqi, Xinjiang 830023, China*

**Yin Yu** − *Xinjiang Academy of Environmental Protection Science, Urumqi, Xinjiang 830011, China; Xinjiang Engineering Technology Research Center for Cleaner Production, Urumqi, Xinjiang 830011, China*

**Yuanyuan Zhang** − *Xinjiang Academy of Environmental Protection Science, Urumqi, Xinjiang 830011, China; Xinjiang Engineering Technology Research Center for Cleaner Production, Urumqi, Xinjiang 830011, China*

Complete contact information is available at: https://pubs.acs.org/10.1021/acsomega.4c02493


### Notes

The authors declare no competing financial interest.

## ■ ACKNOWLEDGMENTS

This work was financially supported by basic scientific research project of nonprofit scientific Research Institutes in Xinjiang Uygur Autonomous Region (grant no. KY2023112).

## ■ REFERENCES


(1) Liu, T.; Xiao, S.; Li, N.; Chen, J.; Zhou, X.; Qian, Y.; Huang, C.-H.; Zhang, Y. Water Decontamination via Nonradical Process by Nanoconfined Fenton-Like Catalysts. *Nat. Commun.* **2023**, *14*, No. 2881.

(2) Jeon, T. H.; Koo, M. S.; Kim, H.; Choi, W. Dual-Functional Photocatalytic and Photoelectrocatalytic Systems for Energy- and Resource-Recovering Water Treatment. *ACS Catal.* **2018**, *8*, 11542−11563.

(3) Park, H.; Park, Y.; Kim, W.; Choi, W. Surface Modification of $TiO_2$ Photocatalyst for Environmental Applications. *J. Photochem. Photobiol., C* **2013**, *15*, 1−20.

(4) Sirtori, C.; Zapata, A.; Oller, I.; Gernjak, W.; Agüera, A.; Malato, S. Solar Photo-Fenton as Finishing Step for Biological Treatment of a Pharmaceutical Wastewater. *Environ. Sci. Technol.* **2009**, *43*, 1185−1191.

(5) Sebai, W.; Ahmad, S.; Brun, N.; Cacciaguerra, T.; Cot, D.; Boccheciampe, A.; Chaurand, P.; Levard, C.; Belleville, M.-P.; Sanchez-Marcano, J.; Galarneau, A. Treatment of Wastewater Containing Pharmaceutical Micropollutants by Adsorption under Flow in Highly Porous Carbon Monoliths. *Chem. Mater.* **2023**, *35*, 8464−8482.

(6) Chong, M. N.; Jin, B.; Chow, C. W.; Saint, C. Recent Developments in Photocatalytic Water Treatment Technology: A Review. *Water Res.* **2010**, *44*, 2997−3027.

(7) Saeed, M. U.; Hussain, N.; Sumrin, A.; Shahbaz, A.; Noor, S.; Bilal, M.; Aleya, L.; Iqbal, H. M. N. Microbial Bioremediation Strategies with

Wastewater Treatment Potentialities − A Review. *Sci. Total Environ.* **2022**, *818*, No. 151754.
(8) Bibi, A.; Bibi, S.; Abu-Dieyeh, M.; Al-Ghouti, M. A. Towards Sustainable Physiochemical and Biological Techniques for the Remediation of Phenol from Wastewater: A Review on Current Applications and Removal Mechanisms. *J. Cleaner Prod.* **2023**, *417*, No. 137810.
(9) Qasem, N. A. A.; Mohammed, R. H.; Lawal, D. U. Removal of Heavy Metal Ions from Wastewater: A Comprehensive and Critical Review. *npj Clean Water* **2021**, *4*, 36.
(10) Li, Q.; Zhang, N.; Yang, Y.; Wang, G. Z.; Ng, D. H. L. High Efficiency Photocatalysis for Pollutant Degradation with $MoS_2/C_3N_4$ Heterostructures. *Langmuir* **2014**, *30*, 8965−8972.
(11) Hoffmann, M. R.; Martin, S. T.; Choi, W. Y.; Bahnemann, D. W. Environmental Applications of Semiconductor Photocatalysis. *Chem. Rev.* **1995**, *95*, 69−96.
(12) Zhao, X.; Zhang, G.; Zhang, Z. $TiO_2$−Based Catalysts for Photocatalytic Reduction of Aqueous Oxyanions: State−of−the−Artand Future Prospects. *Environ. Int.* **2020**, *136*, No. 105453.
(13) Zhang, H.; Gao, Y.; Meng, S.; Wang, Z.; Wang, P.; Wang, Z.; Qiu, C.; Chen, S.; Weng, B.; Zheng, Y.-M. Metal Sulfide S-Scheme Homojunction for Photocatalytic Selective Phenylcarbinol Oxidation. *Adv. Sci.* **2024**, No. 2400099.
(14) Sheng, J.; Li, X.; Xu, Y. Generation of $H_2O_2$ and OH Radicalson $Bi_2WO_6$ for Phenol Degradation under Visible Light. *ACS Catal.* **2014**, *4*, 732−737.
(15) Li, Z.; Cong, S.; Xu, Y. Brookite vs Anatase $TiO_2$ in the Photocatalytic Activity for Organic Degradation in Water. *ACS Catal.* **2014**, *4*, 3273−3280.
(16) Xia, F. N.; Wang, H.; Xiao, D.; Dubey, M.; Ramasubramaniam, A. Two-Dimensional Material Nanophotonics. *Nat. Photonics* **2014**, *8*, 899−907.
(17) Wang, Q. H.; Kalantar-Zadeh, K.; Kis, A.; Coleman, J. N.; Strano, M. S. Electronics and Optoelectronics of Two-Dimensionaltransition Metal Dichalcogenides. *Nat. Nanotechnol.* **2012**, *7*, 699−712.
(18) Xu, M. S.; Liang, T. T.; Shi, M. M.; Chen, H. Z. Graphene-Like Two-Dimensional Materials. *Chem. Rev.* **2013**, *113*, 3766−3798.
(19) Lei, F. C.; Zhang, L.; Sun, Y. F.; Liang, L.; Liu, K. T.; Xu, J. Q.; Zhang, Q.; Pan, B. C.; Luo, Y.; Xie, Y. Atomic-Layer-Confined Doping for Atomic-Level Insights into Visible-Light Water Splitting. *Angew. Chem., Int. Ed.* **2015**, *54*, 9266−9270.
(20) Liang, L.; Zhang, J. J.; Zhou, Y. Y.; Xie, J. F.; Zhang, X. D.; Guan, M. L.; Pan, B. C.; Xie, Y. High-Performance Flexible Electrochromic Device Based on Facile Semiconductor-to-Metal Transition Realized by $WO_3{\cdot}2H_2O$ Ultrathin Nanosheets. *Sci. Rep.* **2013**, *3*, No. 1936.
(21) Chen, X. Y.; Zhou, Y.; Liu, Q.; Li, Z. D.; Liu, J. G.; Zou, Z. G. Ultrathin, Single-Crystal $WO_3$ Nanosheets by Two-Dimensional Oriented Attachment toward Enhanced Photocatalystic Reduction of $CO_2$ into Hydrocarbon Fuels under Visible Light. *ACS Appl. Mater. Interfaces* **2012**, *4*, 3372−3377.
(22) Kong, L.; Yan, J.; Liu, S. F. Carbonyl Linked Carbon Nitride Loading Few Layered $MoS_2$ for Boosting Photocatalytic Hydrogen Generation. *ACS Sustainable Chem. Eng.* **2019**, *7*, 1389−1398.
(23) Huang, X.; Han, X.; Tang, R.; Wu, H.; Chen, S.; Chen, J.; Zeng, Z.; Deng, S.; Wang, J. Anion-Mediated In Situ Reconstruction of the $Bi_2MoO_6$ Precatalyst for Enhanced Electrochemical $CO_2$ Reduction over a Wide Potential Window. *ACS Appl. Mater. Interfaces* **2024**, *16*, 742−751.
(24) Xie, Y.; Shang, X.; Liu, D.; Zhao, H.; Gu, Y.; Zhang, Z.; Wang, X. Non-Noble Metal Thickness-Tunable $Bi_2MoO_6$ Nanosheets for Highly Efficient Visible-Light-Driven Nitrobenzene Reduction into Aniline. *Appl. Catal., B* **2022**, *259*, No. 118087, DOI: 10.1016/j.apcatb.2019.118087.
(25) Bi, J. H.; Wu, L.; Li, J.; Li, Z. H.; Wang, X. X.; Fu, X. Z. Simple Solvothermal Routes to Synthesize Nanocrystalline $Bi_2MoO_6$ Photocatalysts with Different Morphologies. *Acta Mater.* **2007**, *55*, 4699−4705.
(26) Yan, T.; Sun, M.; Liu, H.; Wu, T.; Liu, X.; Yan, Q.; Xu, W.; Du, B. Fabrication of Hierarchical $BiOI/Bi_2MoO_6$ Heterojunction for Degradation of Bisphenol A and Dye under Visible Light Irradiation. *J. Alloys Compd.* **2015**, *634*, 223−231.
(27) Tian, G.; Chen, Y.; Zhou, J.; Tian, C.; Li, R.; Wang, C.; Fu, H. In Situ Growth of $Bi_2MoO_6$ on Reduced Graphene Oxide Nanosheets for Improved Visible-Light Photocatalytic Activity. *CrystEngComm* **2014**, *16*, 842−849.
(28) Yan, T.; Sun, M.; Liu, H. Y.; Wu, T. T.; Liu, X. J.; Yan, Q.; Xu, W. G.; Du, B. Fabrication of Hierarchical $BiOI/Bi_2MoO_6$ Heterojunctionfor Degradationof Bisphenol A and Dye under Visible Light Irradiation. *J. Alloys Compd.* **2015**, *634*, 223−231.
(29) Zou, H.; Dong, X.; Lin, W. Selective CO Oxidation inHydrogen-Rich Gas over $CuO/CeO_2$ Catalysts. *Appl. Surf. Sci.* **2006**, *253*, 2893−2898.
(30) Sharma, M.; Kumar, A.; Gill, D.; Jaiswal, S.; Patra, A.; Bhattacharya, S.; Krishnan, V. Boosting Photocatalytic Nitrogen Fixation via Nanoarchitectonics Using Oxygen Vacancy Regulation in W-Doped $Bi_2MoO_6$ Nanosheets. *ACS Appl. Mater. Interfaces* **2023**, *15*, 55765−55778.
(31) Chai, Y.; Lu, J.; Li, L.; Li, D.; Li, M.; Liang, J. TEOA-Induced In Situ Formation of Wurtzite and Zinc-Blende CdS Heterostructures as A Highly Active and Long-Lasting Photocatalyst for Converting $CO_2$ Into Solar Fuel. *Catal. Sci. Technol.* **2018**, *8*, 2697−2706.
(32) Djokić, V. R.; Marinković, A. D.; Petrović, R. D.; Ersen, O.; Zafeiratos, S.; Mitrić, M.; Ophus, C.; Radmilović, V. R.; Janaćković, D. T. Highly Active Rutile $TiO_2$ Nanocrystalline Photocatalysts. *ACS Appl. Mater. Interfaces* **2020**, *12*, 33058−33068.
(33) Lu, K.-Q.; Li, Y.-H.; Zhang, F.; Qi, M.-Y.; Chen, X.; Tang, Z.-R.; Yamada, Y. M. A.; Anpo, M.; Conte, M.; Xu, Y.-J. Rationally Designed Transition Metal Hydroxide Nanosheet Arrays on Graphene for Artificial $CO_2$ Reduction. *Nat. Commun.* **2020**, *11*, No. 5181.
(34) Rahmani, H.; Mahjoub, A. R.; Khazaee, Z. Bimetallic CuAg Alloyed Nanoparticles Anchored on CdS Nanorods for the photocatalytic Degradation of Enrofloxacin. *ACS Appl. Nano Mater.* **2023**, *6*, 4554−4566.
(35) Momma, K.; Izumi, F. VESTA 3 for three-dimensional visualization of crystal, volumetric and morphology data. *J. Appl. Crystallogr.* **2011**, *44*, 1272−1276.


https://doi.org/10.1021/acsomega.4c02493
*ACS Omega* 2024, 9, 22459−22465